Damage modeling of aluminum casting components considering defect distribution for crashworthiness prediction

Florence Andrieux, Christian Frie, Dong-Zhi Sun

Fraunhofer Institute for Mechanics of Materials IWM

1 Introduction

Aluminum die casting components are widely used in vehicle constructions because of their good compromise between weight reduction and improvement of mechanical properties. The complex geometries of these components with inhomogeneous defect distribution are a relevant issue, as material with higher defect content shows lower fracture strain. It makes the analysis of the damage behavior for crash simulation more challenging. An extensive experimental investigation is required to quantify the scatter as well as the development of a suitable material model to describe it.

The casting alloy Castasil® 37 (AlSi9MnMoZr) is investigated. First, a screening investigation based on tensile tests with specimens cut from different positions of a component together with metallographic and computer tomography (CT) analyses is performed. After segmentation of the fracture surfaces and CT scans the defect distributions are mapped into FE mesh. Moreover, global defect features are extracted from the CT scans and a stochastic model is developed to realize synthetic defect distributions.

A defect dependent material model is derived based on the relationship between defect fraction and elastic, plastic and failure properties and assuming the properties of the defect free material. The model is implemented as User Material Subroutine in the FE program LS-DYNA. The stress state dependent matrix failure strain is calibrated considering the upper bound of the experimental tests on specimens with different geometries. Digital image correlation (DIC) analyses are performed to determine local strains. The model requires a defect distribution as initial condition. Simulation of tensile and bending tests are performed using defect distributions from the fracture surfaces, the CT scans and the stochastic model.

2 Experimental results

To investigate the failure behavior of the aluminum casting alloy Castasil® 37 specimens are cut from a control unit holder. This component has a complex geometry with wall thicknesses ranging from 3 to 10 mm (Fig. 1). A screening investigation based on tensile tests with specimens cut at nine positions of each of six components is performed. To investigate the effect of stress state on failure notched, shear and holed tensile specimens as well as bending and punch specimens are extracted at the position 3 of the component to perform tests inducing different triaxialities.
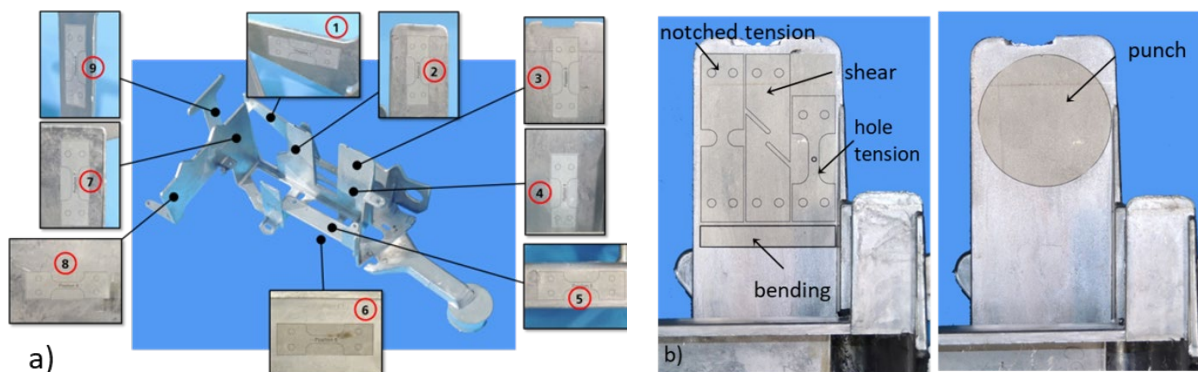

Fig.1: Holder for control units with extraction positions of specimens a) screening tests b) triaxiality tests.

Before tests computer tomography (CT) analyses are done by project partners [1] for some tensile specimens and bending plates. After tests all failure surfaces are analyzed and the defect type and fraction are determined. Four types of defects are found: shrinkage porosity, gas porosity, cold shuts and oxide films. The defects are often found in combination on the failure surface.

Fig. 2 shows the results of the screening tests together with fracture surfaces from stereo microscope.
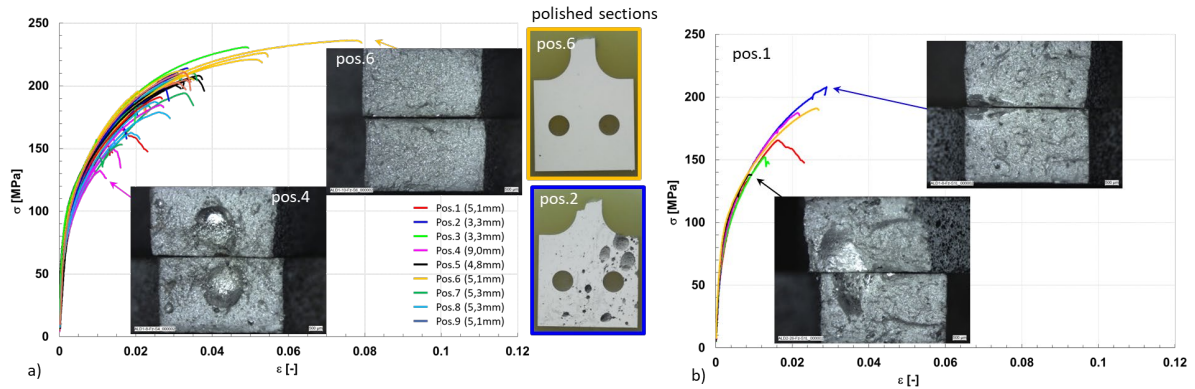

Fig.2: *Nominal stress-strain curves with fracture surfaces and polished sections a) for nine positions b) for position 1.*

There is a pronounced scatter of material properties, especially the failure strain. The failure strain correlates with the defect fraction on the failure surface. The scatter of material properties as an obvious deterministic character with property variations from position to position as shown by Fig.2.a. Position 6 has larger failure strain than position 4. Simultaneously failure surfaces from specimens at position 6 contain few defects but at position 4 many and large defects are observed. Also, the polished sections of the specimen heads at positions 2 and 6 confirm the correlation between defect fraction and failure properties, the position dependency is related to the cast process together with the component geometry. But there is also a stochastic scatter with property variation from component to component for the same position as show by Fig.2.b for the position 1.

For the validation bending tests are performed on plates cut at a position where the highest defect density is expected according to a casting simulation. Plates are cut from the vertical (thickness 7.2 mm) and the horizontal (thickness 4.2 mm) wall. Fig. 3 shows the extraction positions, the experimental set up and flexural stress-strain curves for the bending tests. The bending results confirm the strong scatter of material properties especially the failure strain.
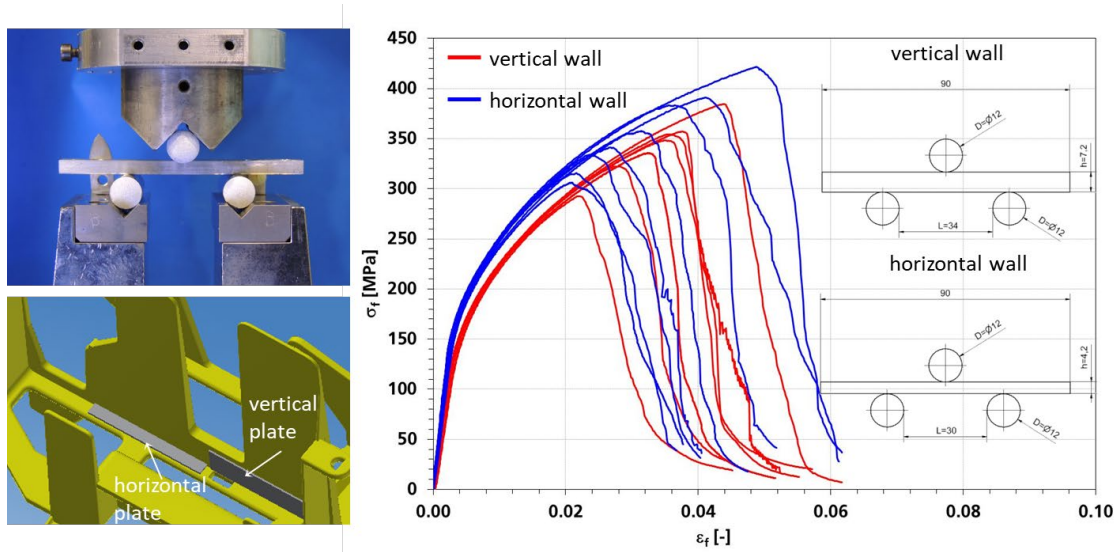

Fig.3: *Flexural stress-strain curves from horizontal and vertical plates (right) with experimental set up and extraction positions of both plates (left).*

The same four types of defects are identified on the failure surfaces of the bending plates as of the tensile specimens. They are also found in combination. The failure strain correlates again with the defect fraction on the failure surface.

3 Defect distributions

To determine the defect distributions, fracture surfaces and CT scans of tensile specimens and bending plates are segmented. Fig.4 shows an original CT scan in RGB color space and the filtered grey level image after a median filter operation. Detail about the segmentation are given in [3].
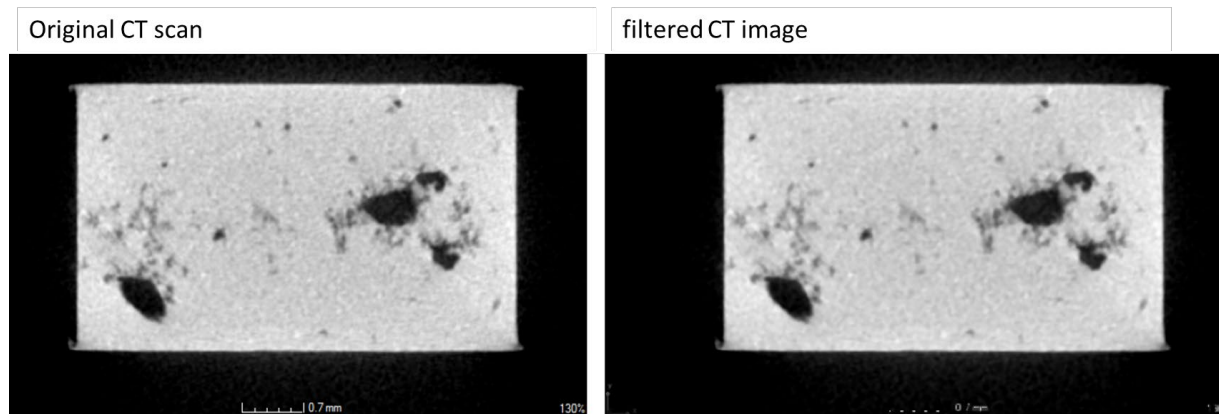

Fig.4:   Original CT scan (left) and the filtered image (right).

3.1   Determination of defect features

For the CT scans, a volume around the location of the failure surface is analyzed. The control volume varies from 3x5x0.8 to 3x5x2.8 mm^3 for tensile specimens and is 40x25x7.2 resp. 40x25x4.2 mm^3 for the vertical resp. horizontal bending plate. From the segmented CT scans, an analysis is performed in order to extract defect features of the control volume. Fig.5 shows the boxplots of the void volume distribution (a) and the percentage of each population to the total porosity (b) for horizontal and vertical bending plates and three components (A, B, C).
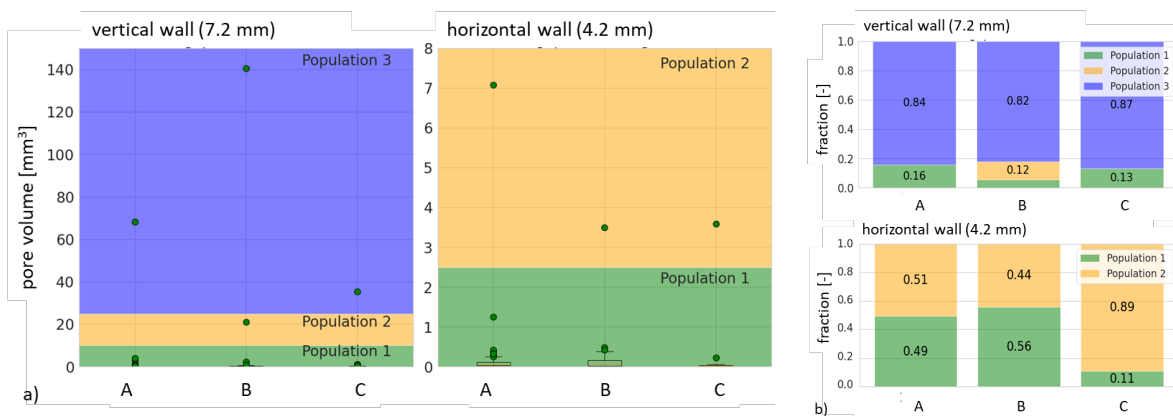

Fig.5:   Arrangement of pores into populations for 2 positions and 3 components a) boxplots b) percentage of each population to the total porosity.

With regard to defect size, the porosity can be split into distinct populations. Fig. 5 confirms that there is a strong influence of the position: vertical and horizontal walls have distinct defect features. The global porosity, the number of populations together with the relative fraction and the defect size of each population are taken as defect features.

3.2 Stochastic model

To generate synthetic defect distributions from a defect feature set into a defined volume, the number of defects for each population is calculated. Moreover, the defects are assumed to be ellipsoidal with a form ratio of 0.5. A centre of an ellipse is randomly chosen until the whole ellipse is located in the volume and no overlapping with other defects occurs. This is realized with a python program [3]. Fig 6 shows a CT scan and two corresponding synthetic distributions.
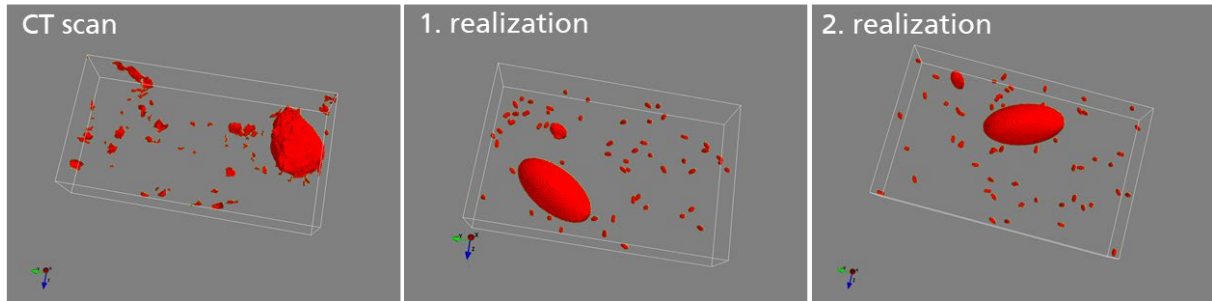

Fig.6: CT scan and two realizations of defect distributions.

Fig.6 illustrates that the stochastic model is suitable to predict a defect distribution representative of the real one. Distribution variations occur within the volume.

4 Simulation

4.1 Material model with defect effect

A material model with influence of defect is developed. The constitutive model described below is a plasticity model with failure criteria [2]. It is characterized by:

- A von Mises yield surface
- A hardening law defined by an extended Voce model (1):

$$\sigma_{y0} = Y_0 + \sum_{i=1}^{2} A_i \left(1 - e^{-B_i \varepsilon_{pl}}\right) \tag{1}$$

- A strain based cumulative damage model [4], the failure strain is given by (2):

$$\varepsilon_{f0} = \begin{cases} d_1 + d_2 \exp(-d_3 \eta) & \eta \geq \eta_{trans} \\ d_{shear1} + d_{shear2} |\eta|^{m_2} + d_{shear3} \langle -\eta \rangle^{m_3} & \eta < \eta_{trans} \end{cases} \tag{2}$$

- The influence of the defect volume fraction on elastic properties (Young's modulus and Poisson's ratio), yield stress and failure strain

In (1) σ_{y0} is the yield stress of the matrix material, ε_{pl} is the von Mises equivalent plastic strain and Y_0, A_i, B_i (i=1,2) are the material parameters of the extended Voce law.

In (2) ε_{f0} denotes the failure strain of the matrix depending on stress triaxiality $\eta = \sigma_{kk}/(3\sigma_e)$. At high triaxiality a Johnson-Cook failure strain is used and at low triaxiality an empirical polynomial function is defined for shear failure. η_{trans} is a transition triaxiality between ductile and shear failure. In (2) <.> denotes the Macaulay brackets. The failure strain is described by 9 material parameters d_1, d_2, d_3, η_{trans}, d_{shear1}, d_{shear2}, d_{shear3}, m_2 and m_3.

CT scans revel inhomogeneous repartition of defects (Fig.7).

Fig.7:   Two CT scan views of a tensile specimen with superimposed FE mesh.

The morphology and spatial arrangement of defects cannot be described at the element level of the FE model but at the specimen level. For this reason, the effect of defect is only accounted for by the porosity, the effect of defect size, form, distance… results indirectly from the defect distribution. It is worth noting that the voids are not modeled explicitly to reduce the computation time. Moreover, due to the different defect sizes such a modeling would involve strongly different element sizes and could not be applied in a component simulation. Indeed, the defect dependent material model is proposed.

The defect fraction reduces the elastic, plastic and failure properties. Fig.8 shows the Young's modulus E, the elastic Poisson's ratio ν, the yield stress σ_y and the failure strain ε_f vs. defect fraction f with the corresponding analytic forms. E_0, ν_0 σ_{y0} and ε_{f0} design the properties of the defect free matrix material, a_x, b_x and c_x (x=E, P, Y or F) are seven material parameters determining the influence of defect on mechanical properties. The porosity f is stored as history variable, its value has to be initialized for each element through initial condition definition using the card `*INITIAL_STRESS_SOLID`. It is worth noting that no defect evolution is considered so that its value is constant. This hypothesis is acceptable because the strain level remains low (under 0.1) and no pronounced necking occurs during a smooth tensile test (see Fig.2) so that no significant void growth is expected.
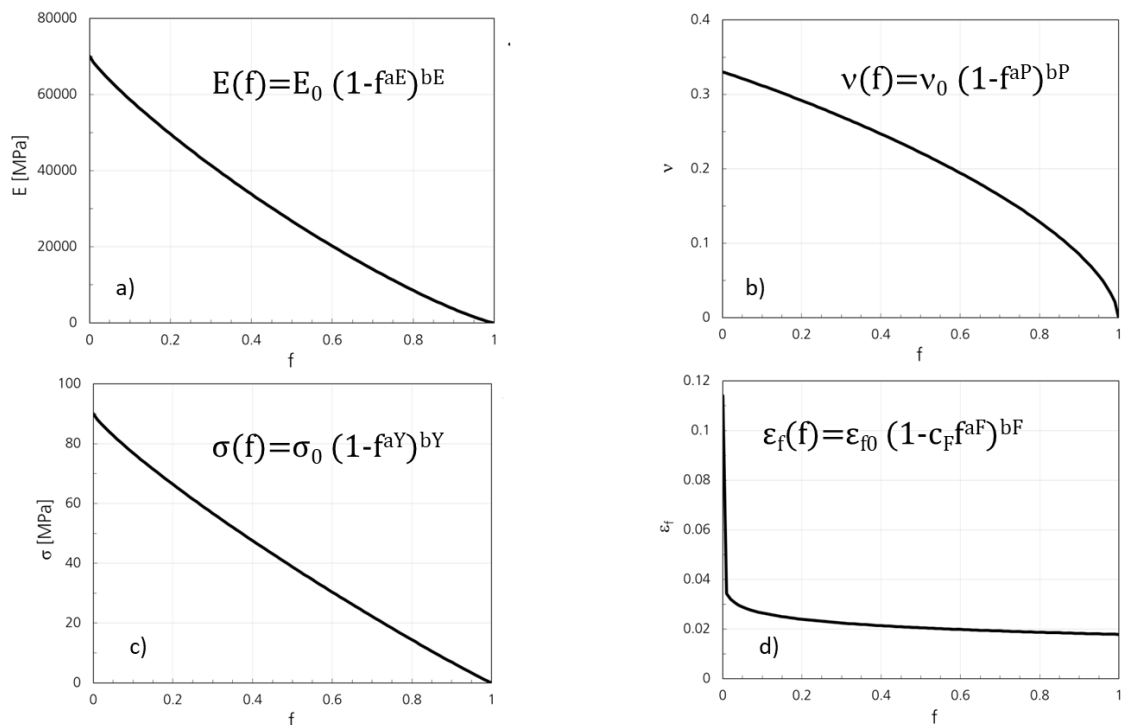

Fig.8:   Young's modulus E (a), the elastic Poisson's ratio ν (b), the yield stress σ_y (c) and the failure strain ε_f (d) vs. defect fraction f with the corresponding analytic forms.

The model is implemented as user material subroutine in the finite element code LS-DYNA.

4.2   Mapping

The defect distributions obtained from the segmented fracture surfaces, the CT scan volumes and the synthetic realizations are homogenised. A mesh is superimposed on the segmented figure and for each element, the proportion of defect is calculated. These results are mapped into the FE mesh as illustrated by Fig.9 in case of a distribution obtained from a fracture surface. Only the region where the defect distribution is investigated needs to be mapped into the FE mesh. From the fracture surface, only one element layer can be defined. Segmentation, homogenization and mapping are realized through Python scripts.
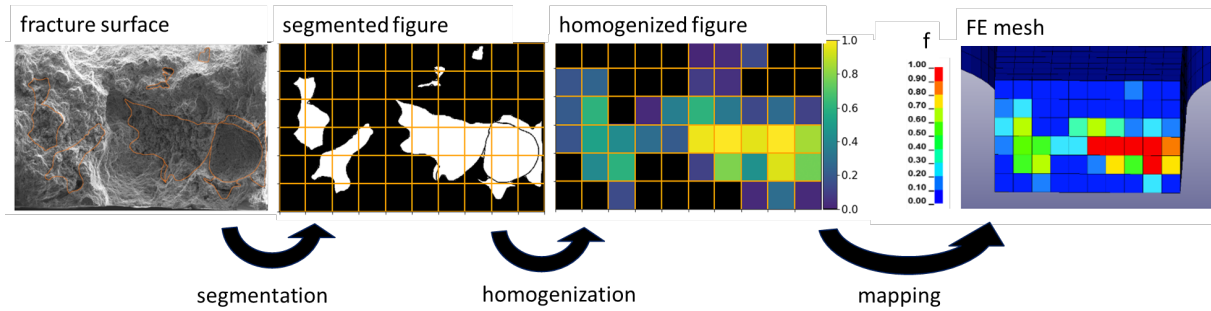

Fig.9:   Mapping method.

Fig.10 gives the defect distribution obtained from a CT scan and two synthetic realizations. All matrix elements with null porosity are removed. The defect distributions well capture the real spatial arrangement of defects in an average manner.
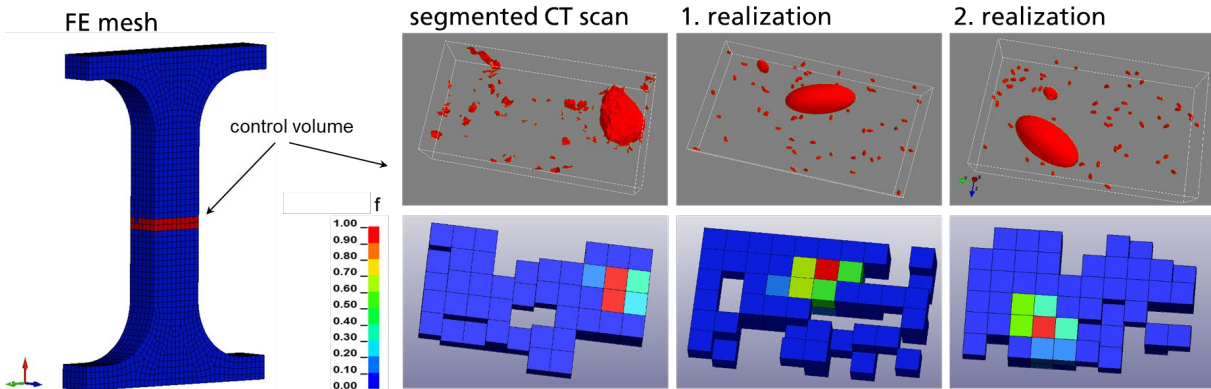

Fig.10: FE mesh from tensile specimen with the control volume (left). Control volume and corresponding defect distribution (right).

4.3   Matrix properties

To determine the stress state dependent matrix failure strain, specimens with different geometries extracted at the same position in a component are tested and the model for the matrix properties is calibrated considering the upper bound of the experimental results. Digital image correlation (DIC) analyses are performed to determine local strains. The matrix failure strain with the loading paths from the six specimens used for the calibration is given in Fig.11. With this curve, it is possible to well predict the global behavior of the specimen tests as shown by Fig.12 in case of a shear test.
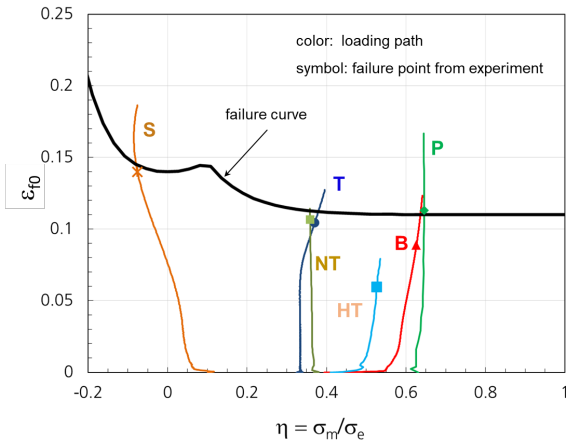
Fig.11: Matrix failure strain with loading paths from shear (S), tensile (T), holed tensile (HT), notched tensile (NT), bending (B) and punch (P) tests.
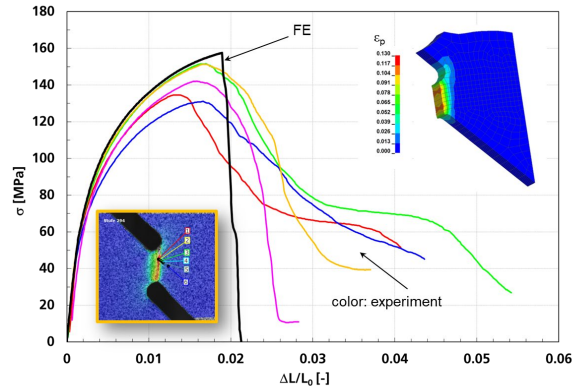
Fig.12: Experimental and simulated normalized force displacement curves from shear tests with strain distribution from DIC analysis and plastic strain distribution in the shear ligament from FE.

In Fig.12 an abrupt force reduction is predicted instead of the gradual experimental one. It is due to the facts that a failure model without coupling stress with damage variable is used and that the element size is almost coarse (0.5 mm).

4.4   Simulation of tests

Tensile tests and bending tests are simulated using defect distributions from fracture surfaces, CT scans and realizations with the stochastic model. The parameters a_F, b_F and c_F (equation in Fig.13) for the porosity dependency of failure stress are calibrated iteratively from the simulation of tensile tests at nine positions using the defect distributions from fracture surfaces.
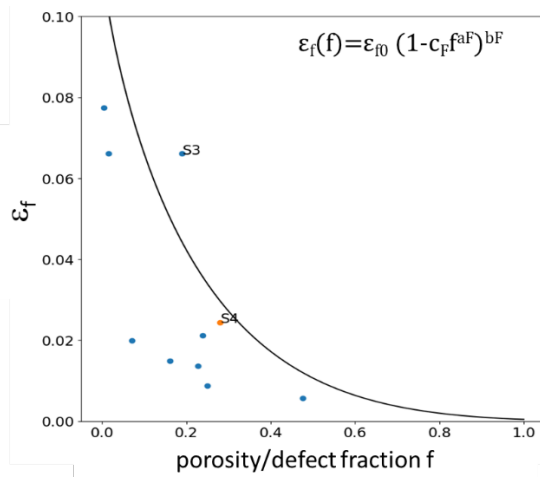

$$\varepsilon_f(f) = \varepsilon_{f0}\,(1 - c_F f^{aF})^{bF}$$

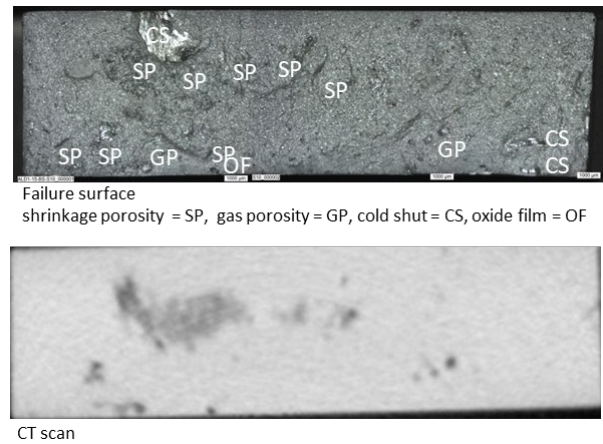*Fig.13: Failure strain vs. defect fraction with experimental points.*

Fig.14: Fracture surfaces with defect annotation and CT scan from a bending plate

Fig.15 compares the experimental stress strain curves with the simulations after mapping of defects obtained from the segmented fracture surfaces for eight positions. The scatter of the failure strain due to the position dependent defect density is well captured by the model.

Fig.16 to 18 compare for three positions the experimental stress strain curves with the simulations after mapping of defects obtained from the segmented fracture surfaces, the CT scan volumes and the

synthetic realizations. The global porosities determined from the CT scanned volumes are indicated. For position 8 (Fig.18) a simulation with the homogeneous distributed global porosity of 11.2% is added.
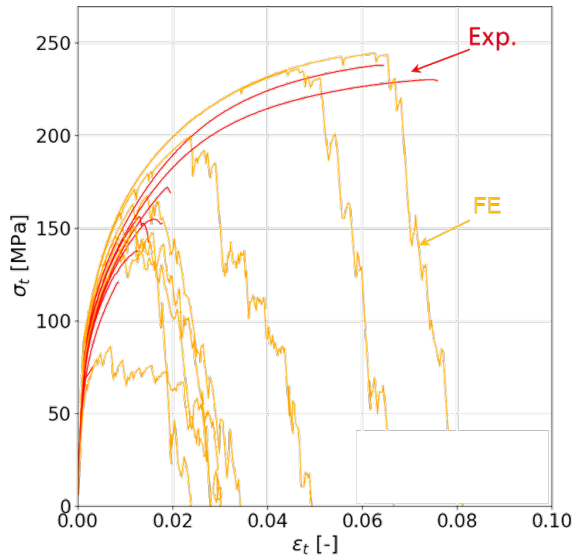

Fig.15: Experimental (red) and calculated (yellow) nominal stress-strain curves for eight positions.
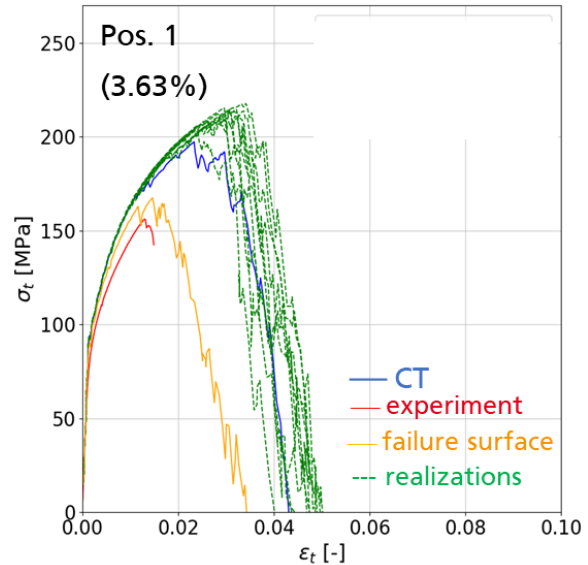
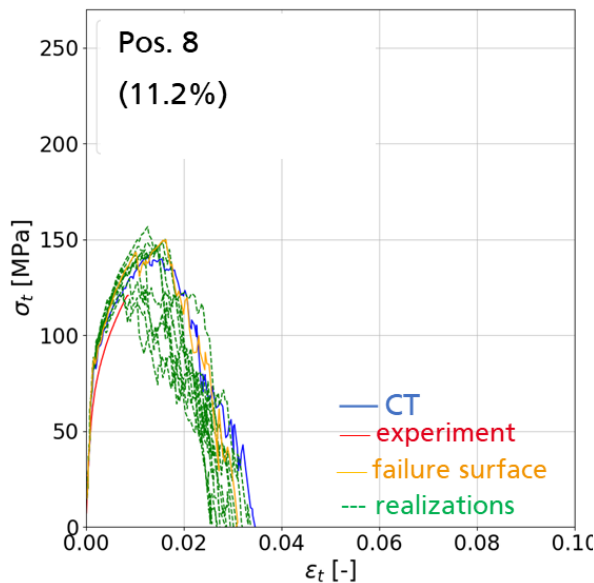*Fig.16: Experimental and calculated nominal stress-strain curves for position 1.*

Fig.17: Experimental and calculated nominal stress-strain curves for position 8.
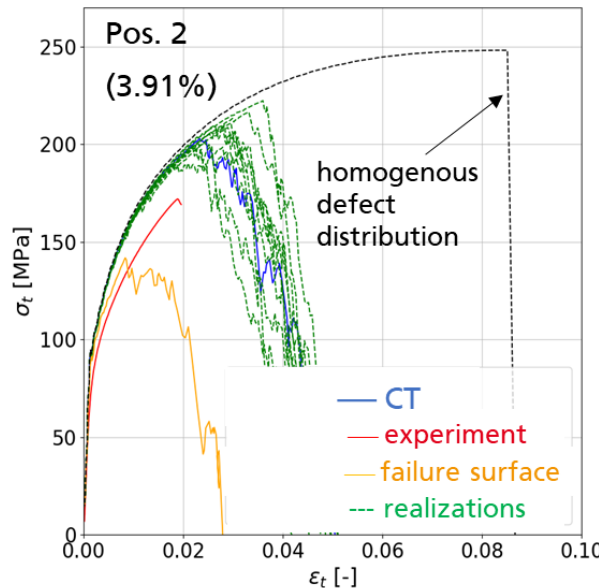
Fig.18: Experimental and calculated nominal stress-strain curves for position 2.

The simulations with the defect distribution from CT always overestimate the ones with the defect from failure surfaces (Fig.16 to 18). It is because CT is not able to detect all defects. Especially the 2-dimensional defects like cold shuts or oxide films are missed from CT. This is illustrated by Fig.13 with comparison of the failure surface and the CT image selected at the same position of a bending plate. The defect types from CT are annotated. Obviously, the CT overlooks the cold shuts and oxide films. The simulations with ten realizations lead to a large scatter of the failure strains, which are obtained from the same defect feature. It shows the importance of the defect arrangement within the volume. This explains the property variations from component to component for a same position (Fig.2.b) due to different arrangements of the defects within the volume. Assuming a homogenous defect distribution

the failure strain is largely overestimated (Fig.18). Keeping in mind that the determination of the defect distributions is subjected to strong uncertainty factors (for example: annotation of defect, scan resolution, choice of threshold by segmentation, location and form of the fracture surface, …) the proposed method is adapted to describe the observed scatter of properties.

Simulations of bending tests are performed with the parameters calibrated from tensile tests to validate the method. Fig.20 compares for a horizontal plate with thickness 7.2 mm the experimental flexural stress strain curve with the simulations after mapping of defects obtained from the segmented fracture surface, the CT scan volume and the ten synthetic realizations. Fig. 19 shows a CT scan, one realization and the porosity distribution in the FE mesh.
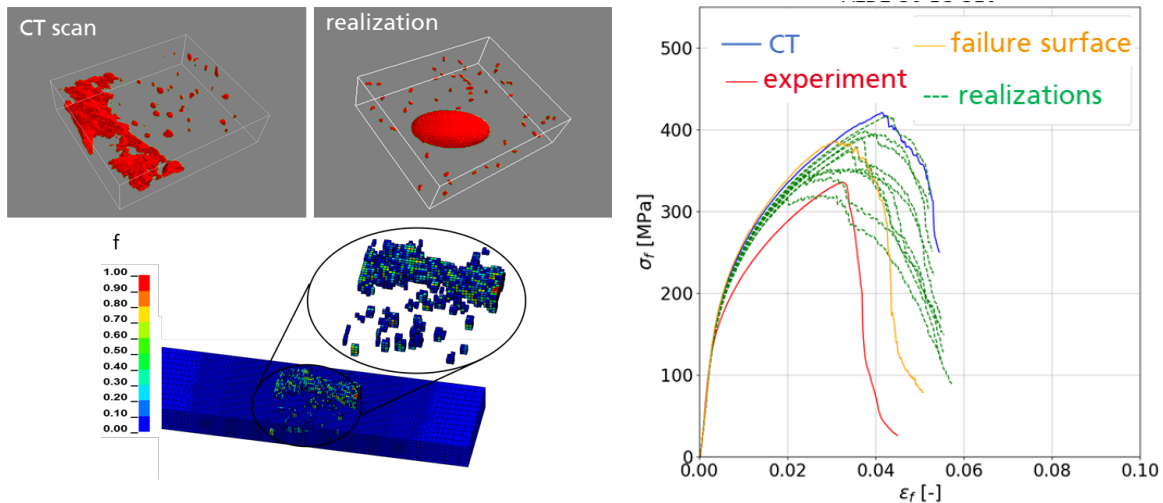

Fig.19: CT scan, one realization and porosity distribution in the FE mesh.

Fig.20: Experimental and calculated flexural stress-strain curves.

The results of the bending tests validate the proposed method. Considering the incertitude of the defect distribution obtained from failure surfaces and CT scans, the parameters calibrated from tensile tests can be accurately transferred to the bending tests. With the defect distribution from CT the failure strain is overestimated since some defects are missed. A large scatter of the failure strain is obtained with different realizations of the same defect feature. It is worth noting that in case of bending tests if the result with the distribution from the CT scan stays in the range of the realizations, it lies on the upper bound. This effect is attributed to the idealization of the voids as ellipsoid in the synthetic realizations. Fig.19 shows that indeed the big defect has an irregular form with a corresponding higher surface for the same volume. This strong idealization of the voids as ellipsoid leads to an overestimation of the defect severity and could be released using a more sophisticated defect description [3].

5 Summary

The casting alloy Castasil® 37 was investigated. There is a pronounced scatter of material properties, especially the failure strain. It can be correlated with the inhomogeneous distribution of microdefects observed on fracture surfaces or on CT scans.
Fracture surfaces and CT scans were segmented. From global defect features extracted from the CT scans a stochastic model was developed to realize synthetic defect distributions. All these defect distributions are mapped into FE meshes. A material model was developed in which the defect fraction reduces the mechanical properties. It is shown that the developed method well captures the deterministic and stochastic scatter of local material properties. However, its accuracy remains subjected to the accuracy of the microdefect distribution determination or prediction.
Coupling of casting simulation with crash simulation is a necessary step to solve the problem.

6 Literature

[1]   Sun, D.-Z., Lehmus, D.: "Modellierung der Einflusse von Mikrodefekten auf das Versagensverhalten von Al-Druckgusskomponenten mit stochastischem Aspekt für die Crashsimulation", FAT-Schriftenreihe 338, 2020

[2]   Sun, D.-Z., Burblies, A.: "Modellierung der Einflusse von Porenmorphologie auf das Versagensverhalten von Al-Druckgussteilen mit stochastischem Aspekt für durchgängige Simulation von Gießen bis Crash", FAT-Schriftenreihe 277, 2015

[3]   Frie, C.: "Versagensmodellierung von Aluminiumguss unter Berücksichtigung von CT-Bildern und metallographischen Analysen", Masterarbeit, IWM, 2020.

[4]   Sun, D.-Z., Andrieux, F., Feucht, M.: "Simulation of the process chain from forming to crash taking into account stochastic aspects ", Procs. 9th LS-DYNA Users' Conference, Bamberg, Germany, 2010.